Composites: Part A 210 (2026) 110083

Contents lists available at ScienceDirect

Composites Part A

journal homepage: www.elsevier.com/locate/compositesa

Programmable, fluorescent and shape-changing composite fibers for Fe^{3+} detection and filtration

Yiling Yu [a], Tao Guo [a], Lan Luo [a], Linlin Wang [a,*], Fenghua Zhang [a,*], Yanju Liu [b], Jinsong Leng [a]

[a] Centre for Composite Materials and Structures, Harbin Institute of Technology (HIT), Harbin 150080, the People's Republic of China
[b] Department of Astronautical Science and Mechanics, Harbin Institute of Technology (HIT), Harbin 150001, the People's Republic of China

ARTICLE INFO

Keywords:
Shape memory polymers
Fluorescent polyurea
Composite fibrous membranes
Fe^{3+}detection

ABSTRACT

Simultaneous detection and removal of excess Fe^{3+} is essential for ecological balance, food safety, and pathology, yet despite the promising stability of specific fluorescent functional materials, their conventional direct dispersion in aqueous solution causes structural instability, secondary pollution, and a lack of integration between detection and removal. To overcome these limitations, we developed a programmable, fluorescent, and shape-changing composite fiber for Fe^{3+} recognition, detection, and removal in a single platform. Composite fibers are prepared by combining fluorescent particles with thermally responsive fibers via electrostatic forces. The fibers have stable fluorescent properties and can detect Fe^{3+} with high selectivity and sensitivity. Upon thermal stimulation, it undergoes reversible shape programming and recovery, enabling a structural transition from random to aligned at the microscale. This smart structural modulation enhances specific surface area and pore distribution, thereby improving Fe^{3+} detection and adsorption capacity. The programmable fiber exhibits selective fluorescence quenching within 5 s and achieves up to 98 % Fe^{3+} removal efficiency through shape-changing composite fiber. Our work provides a novel and sustainable strategy for large-scale management, addressing the dual need for Fe^{3+} detection and filtration in modern smart water treatment systems.

1. Introduction

Fe^{3+} plays an essential role in biochemical processes, but excessive concentrations beyond a certain threshold pose significant threats to aquatic ecosystems and human health [1–11]. Therefore, the development of effective technologies for Fe^{3+} monitoring and removal remains of critical importance.

Conventional analytical techniques, including atomic absorption/emission spectroscopy and inductively coupled plasma mass spectrometry [12–14], offer high sensitivity, they typically require expensive equipment and offline analysis, hindering on-site and continuous monitoring [12–15]. Fluorescent chemical sensors have gained attention owing to their high sensitivity, rapid response, and operational simplicity [8,16]. But these sensors typically provide identification/quantification signals without enabling pollutant removal, thereby separating detection from treatment [17,18]. Accordingly, although laboratory analytical techniques achieve high sensitivity and accuracy, they remain confined to detection and cannot directly remove Fe^{3+} from water. Consequently, the fundamental bottleneck in current Fe^{3+} water treatment lies in the functional separation of detection and removal processes [19,20].

Electrospinning employs electrostatic forces to fabricate continuous fibers with diameters ranging from microscale to nanoscale [21–32]. Due to their high specific surface area and porous structure, functional electrospun fibers can enable effective pollutant enrichment [33,34]. Electrospun fibers have gained recognition for their applications in pollutant detection, filtration, chemical separation, and contaminated water filtration [35]. However, conventional electrospun filtration membranes generally lack intrinsic, selective Fe^{3+} recognition capabilities, limiting their ability to simultaneously monitor and remove pollutants [36]. This functional disconnection leads to blind treatment processes, delayed efficiency assessments, and uncertainties in resource regeneration, severely hindering the development of intelligent, precision water treatment systems. To overcome this limitation, there is an urgent need to develop novel materials that integrate detection and filtration functionalities. Stimulus-responsive materials offer a highly

* Corresponding authorsat: Centre for Composite Materials and Structures, Harbin Institute of Technology (HIT), Harbin, 150080, the People's Republic of China.
E-mail addresses: wangll_hit@163.com (L. Wang), fhzhang_hit@163.com (F. Zhang).

https://doi.org/10.1016/j.compositesa.2026.110083
Received 15 May 2026; Received in revised form 21 June 2026; Accepted 3 July 2026
Available online 4 July 2026
1359-835X/

promising solution, capable of producing intuitive signal changes such as color shifts and fluorescence [18,37–41]. When exposed to external stimuli like heat, light, or electricity, shape memory polymers in particular can exactly return from a transitory shape to their pre-deformation.

In this work, we proposed and fabricated a novel shape-memory fluorescent fiber, in which fluorescent polyurea (PU) particles with specific Fe^{3+} response was uniformly loaded onto shape-memory polylactic acid (PLA)/tributyl citrate (TBC) fibers via electrospinning. This design integrated two major functions: upon binding of Fe^{3+} with the characteristic functional groups in the PU particles, a rapid and visually detectable fluorescence quenching effect is triggered under 365 nm UV light. Leveraging the well-preserved shape-memory effect of PLA fibers over multiple cycles, the microstructure of the fibers can be reconfigured to achieve efficient and selective adsorption and removal of Fe^{3+}, thereby avoiding secondary pollution of water (Fig. 1). This study not only provides an innovative integrated detection-removal material for Fe^{3+} contamination control in water, but also offers a new design strategy and technical reference for developing multifunctional water treatment materials targeting other pollutants.

2. Material and methods

2.1. Materials

All reagents and solvents were used as received without any purification. Isophorone diisocyanate (IPDI), diethyl methyl benzene diamine (DETDA), *N, N'*-dimethylformamide (DMF), toluenediisocyanate (TDI), and deuterated DMSO-d_6 were purchased from Shanghai Aladdin Biochemical Technology Co., Ltd. Acetone was purchased from Tianjin Fuyu Fine Chemicals. Deionized water, polylactic acid (PLA), and tributyl citrate (TBC) were laboratory-made. Potassium bromide (KBr, SP) was purchased from Shanghai Macklin Biochemical Co. Ltd.

2.2. Preparation of PU particles

A mixture of H_2O-acetone (90.0 g) at a mass ratio of 3/7 was first charged into a 250 mL high-borosilicate glass bottle. IPDI (57.4 mmol) was added at a rate of 5 mL min^{-1} under stirring at 100 rpm at 30 °C. The polymerization was allowed to continue overnight after the reactant addition was completed, followed by centrifugation to separate the solid at 3,000 rpm at −5 °C, and the resulting solid was dried at 70–80 °C under vacuum obtain a white powder product, i.e., the PU particles (PUP0). PUP1 and PUP2 were synthesized as described above. Specifically, under these reaction conditions, IPDI and DETDA were separately added slowly into the reaction system at a feeding rate of 5 mL min^{-1}. For the synthesis of PUP2, TDI was used as the reactant.

2.3. Preparation of shape memory composite fibers

PLA and TBC were mixed at a mass ratio of 5:1, and dichloroethane was added to prepare a transparent solution with a mass fraction of 9 %. The electrospinning parameters were set as follows: a 21G needle paired with a 20 mL syringe was used, the flow rate was 1 mL h^{-1}, a voltage of 20 kV was applied, the distance between the needle and the collector was 10–15 cm, and electrospinning was conducted for 6 h to obtain a pristine scaffold named PLA/TBC. Separately, PUP powder was dispersed in a DMF/H_2O mixed solvent at a volume ratio of 9:1 to prepare a 100 mg mL^{-1} suspension, which was uniformly dispersed by ultrasonic treatment for 2 h. A 18G needle paired with a 20 mL syringe was used, the flow rate was 1.5 mL h^{-1}, a voltage of 18–20 kV was applied, the distance between the needle and the collector was 10–15 cm. Subsequently, the particles were loaded onto the PLA/TBC fibers via electrospraying to fabricate the fluorescent fibrous membranes within 45 min. Based on the electrospinning of a 9 wt% PLA/TBC solution and the electrospraying of a 100 mg mL^{-1} PUP suspension, the composite fibrous membrane exhibited an estimated PLA/TBC-PUP mass ratio of 4.8:1, which was approximated as 5:1 in terms of the overall solid composition. After electrospray deposition, the fiber membranes were treated using a plasma cleaner (PELCO easiGlow) at a discharge current of 15 mA and a chamber pressure of 0.26–0.54 mbar for 3 min to improve the surface wettability.

2.4. Molecular structure and microstructural characterization

Fourier transform infrared (FTIR) spectra were recorded with a Spectrum Two DGTS instrument (Perkin-Elmer, MA, USA) by placing the powders of PUP0, PUP1, and PUP2, and the fibrous membranes of PLA/TBC, PTP0, PTP1, and PTP2 on a KBr pellet. The chemical structures of PUP0, PUP1, and PUP2 powders were characterized by ^1H NMR spectroscopy using an Avance III 400 MHz spectrometer (Brüker) with DMSO-d_6 as the solvent. A crosshead speed of 10 mm min^{-1} was applied to generate the stress–strain curve.

Scanning electron microscopy (SEM) and energy-dispersive spectroscopy (EDS) images were obtained using a Schottky field emission scanning electron microscope (SU5000). PLA/TBC, PTP0, PTP1, and

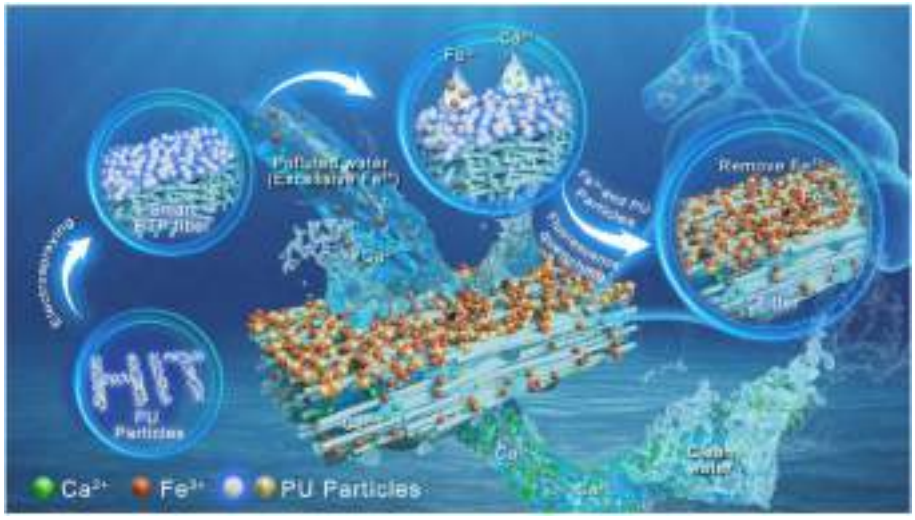

Fig. 1. A schematic diagram showing the fabricating process of smart PTP fibrous membranes, where PU particles are uniformly distributed among electrospun fibers to synergistically combine Fe^{3+} detection and filtration.

PTP2 fibrous membranes were placed under an optical microscope (DeLang Optical Instruments Co., Ltd., Shangrao, Jiangxi, China) for observation and photography. XPS measurements were performed on a Thermo Scientific K-Alpha X-ray photoelectron spectrometer (Thermo Fisher). The base pressure in the analysis chamber was approximately 5 × 10^{-9} mbar. A monochromatic Al Kα X-ray source (hv = 1486.6 eV) was operated at 12 kV and 6 mA. The sample was weighed, degassed at 30 °C under vacuum for 1 h, and analyzed by nitrogen physisorption at 77 K using an automated BET surface area analyzer. The water contact angle was measured using a contact angle/surface tension measuring instrument (Shanghai Xuanzhun SZ-CAMC32).

2.5. Thermal performance testing

Differential scanning calorimetry (DSC) measurements of PLA/TBC, PTP0, PTP1, and PTP2 scaffold samples were performed using a Mettler-Toledo DSC ISTARe instrument. The sample mass was precisely controlled within the range of 5–10 mg. All tests were conducted under a nitrogen atmosphere with a heating rate of 10 °C min^{-1}, scanning from 0 °C to 180 °C. Thermogravimetric analysis (TGA) tests of PLA/TBC, PTP0, PTP1, and PTP2 fibrous membranes were carried out on a Mettler-Toledo TGA/DSC STARe System at a heating rate of 10 °C min^{-1} from 25 °C to 500 °C in air.

2.6. Dynamic thermomechanical analysis

The temperature range of the DMA test was 25–80 °C, the heating rate was 5 °C min^{-1}, and the test frequency was 1 Hz. The shape fixation ratio (R_f), shape recovery ratio (R_r), and recovery rate of the samples were determined during the shape memory performance tests. In the equations (1–2), θ_0 represents the angle of the strip bent into a "U" shape, θ_f denotes the change in bending angle before and after shape fixation, and θ_1 indicates the change in bending angle before and after shape recovery.

$$R_f = \frac{\theta_0 - \theta_f}{\theta_0} \times 100\% \quad (1)$$

$$R_r = \frac{\theta_0 - \theta_1}{\theta_0} \times 100\% \quad (2)$$

2.7. Fluorescence performance test

The ultraviolet–visible (UV–Vis) absorption spectra of PUP0, PUP1, and PUP2 powders were measured using a UV-3101PC spectrophotometer (Shimadzu, Japan) with a wavelength scanning range of 200–600 nm and a slit width of 8 nm. Additionally, the UV–Vis absorption spectra of the materials were recorded at room temperature using a Lambda 35 spectrophotometer (PerkinElmer, USA) with a wavelength scanning range of 200–600 nm and a slit width of 2 nm. The solid-state fluorescence excitation and emission spectra of PUP0, PUP1, and PUP2 powders were obtained using an F-7000 fluorescence spectrophotometer (Hitachi, Japan) with both excitation and emission slit widths set at 2.5 nm. The absolute photoluminescence quantum yields of PUP0, PUP1, and PUP2 powders were determined using an FLS 920 steady-state/transient fluorescence spectrometer (Edinburgh Instruments, UK) equipped with an integrating sphere attachment.

2.8. Mechanical testing and filtration experiments of the different fibrous membranes

PLA/TBC, PTP0, PTP1, and PTP2 were cut into parallel samples with a length of 30 mm and a width of 15 mm, and the thicknesses of the different samples were measured by digital calipers with a precision of 0.01 mm. The Young's modulus, maximum stress, and strain at break of the different fibrous membranes were tested using a tensile testing machine and were obtained from triplicate samples in each group.

The removal efficiency (*RE*) was determined by equation (3), as described by Costa and co-workers.

$$RE = \frac{C_0 - C_e}{C_0} \times 100\% \quad (3)$$

where C_0 is the initial concentration of metal in the solution (mmol L^{-1}), and C_e is the concentration of metal at the equilibrium (mmol L^{-1}).

3. Results

3.1. Preparation and structural characterization of the PU particles

To address the critical need for detecting excessive Fe^{3+} concentrations in polluted water, the synthesized materials were designed to exhibit specific detection capabilities. The fluorescent PU particles exhibit highly selective fluorescence quenching in the presence of ferric ions [42]. The isocyanate groups of isophorone diisocyanate reacted with water to form urea linkages, which constitute the core reaction for PUP0 formation. The synthesis of PUP2 followed a similar approach to that of PUP1, where the isocyanate groups of toluene diisocyanate reacted with water to form urea linkages. During PUP1 synthesis, a rigid structure and a urea-bond constraint system were introduced that restricted molecular motion upon aggregation, resulting in luminescence (Fig. 2a-b). Furthermore, the isocyanate-amine addition reaction yielded urea-based products containing rigid and hydrogen-bonded structures. The combined rigidity and constraints ensured luminescence across all synthesized variants while maintaining the essential properties required for specific detection.

The chemical compositions of the synthesized PUP0, PUP1, and PUP2 were characterized by FTIR spectroscopy (Fig. S1). No characteristic absorption peak corresponding to the the stretching vibration of the isocyanate groups was observed in the range of 2,280–2,240 cm^{-1}, indicating complete consumption of the –NCO groups during polymerization. The absorption band at approximately 3,360 cm^{-1} was assigned to N–H stretching vibration, while the peaks at around 1,655 cm^{-1} and 1,540 cm^{-1} corresponds to the C=O stretching vibration and C-N stretching vibration of the urea groups, respectively. In addition, the peaks located at 2,888 cm^{-1} and 2,965 cm^{-1} were attributed to the symmetric and asymmetric stretching vibrations of C–H bonds.

The chemical structures of the obtained polymers were further confirmed by^1H NMR spectroscopy (Fig. 3a). The hydrogen protons of the –NH-CO-NH- urea linkage consistently resonated within the chemical shift range of 6–9 ppm, which is characteristic of PU structures. The chemical shift of protons in the terminal primary amino group (–NH_2) was influenced by the adjacent substituent groups, with aliphatic terminal groups exhibiting lower chemical shift values and aromatic terminal groups showing relatively higher chemical shifts. These results collectively verified the successful synthesis of the designed fluorescent PU. In addition to contributing to the luminescent properties, the urea groups provide potential coordination sites for Fe^{3+} ions, which is beneficial for fluorescence-based sensing applications. Morphological characterization revealed that PUP0, PUP1, and PUP2 possessed relatively smooth surfaces with average particle diameters of 3.62 ± 1.10, 0.76 ± 0.22, and 1.21 ± 0.48 μm, respectively (Fig. 3b-c). Thermogravimetric analysis demonstrated that PUP1 exhibited an initial decomposition temperature of approximately 300 ℃, which is substantially higher than the sterilization temperature commonly used for biomedical materials (121.3 ℃), indicating sufficient thermal stability for potential biomedical conditions (Fig. S2).

3.2. Fluorescent properties of the PU particles

PU particles exhibited fluorescence in the visible light region when observed in their solid state. PUP0, PUP1, and PUP2 were systematically

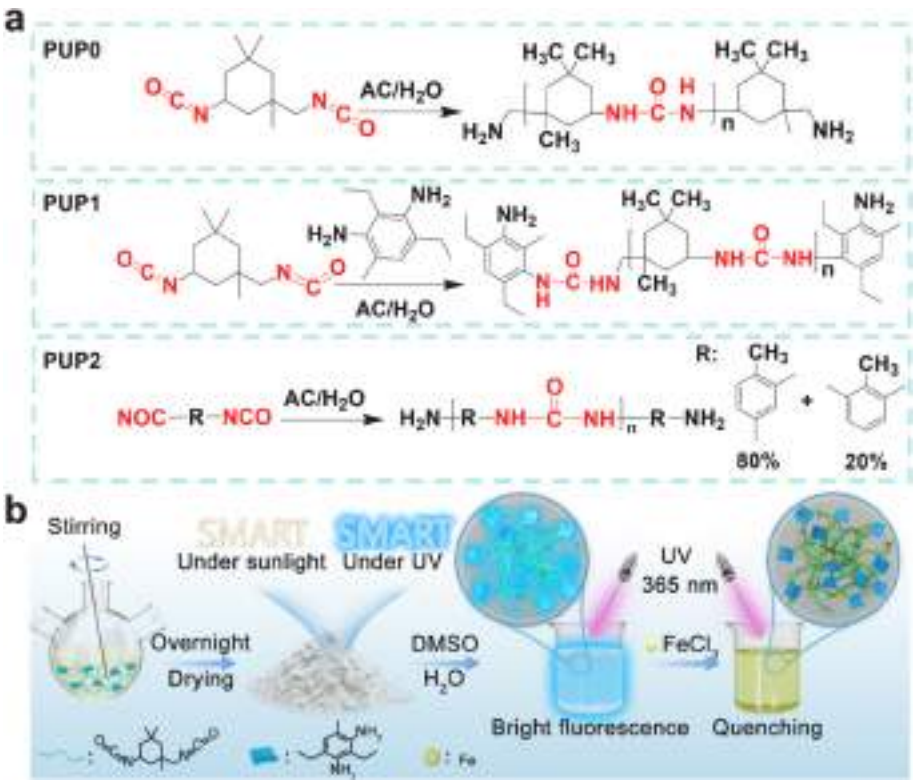

Fig. 2. Preparation and structural characterization of the PUP. (a) Molecular structure design diagram of PUP0, PUP1, and PUP2. (b) Preparation diagram of PUP1.

investigated using UV–Vis absorption spectroscopy and fluorescence emission spectroscopy. The solid PUP0, PUP1, and PUP2 exhibited fluorescence emission in the visible region and fluorescent properties (Fig. 4a). Compared to PUP0 and PUP2, the fluorescence spectrum of PUP1 exhibits a distinct peak at approximately 425 nm under a 365 nm excitation wavelength. Spectral analysis indicates that the emission peak intensity increases with increasing excitation wavelength, and the main emission peak of PUP1 red-shifts from 425 nm to 448 nm (Fig. 4a-b). In the UV–Vis absorption spectrum, PUP1 exhibited a shoulder peak at approximately 345 nm (Fig. 4c). This absorption band is attributed to the n → π* transition of the carbonyl (C=O) group, which indicates the presence of abundant oxygen-containing functional groups in the PUP1 structure. Furthermore, under 365 nm UV light irradiation, both the powder form and aqueous solution of PUP1 displayed bright blue luminescence (Fig. 4d-e). π–π stacking is a noncovalent interaction, with strong π–π stacking effects occurring between urea groups [18,43]. These observations suggested that the luminescence behavior of PUP1 was closely associated with its oxygen-containing functional groups, implying that its emission mechanism may not be solely dominated by the conventional π–π* transition of the aromatic backbone.

The –NH-CO-NH- urea linkage inherent in the PU structure contains π-electrons, enabling intermolecular interactions with rigid cyclic structures. The quantum yield of PUP1 reaches 33 %, which is significantly higher than that of PUP0 and PUP2 (Table S1). The planar rigid conjugated structure in PU, through covalent cross-linking between rigid domains, restricts non-radiative transitions while enhancing radiative transitions. This enables the material to exhibit intense and stable blue fluorescence under 365 nm ultraviolet light [44]. Compared with PUP0 and PUP2, the urea bonds in PUP1 interact with the rigid benzene ring structure, which may lead to increased steric hindrance and thereby generate fluorescence emission. PU particles, whether in solid or liquid form, exhibit rapid and stable fluorescence when excited by 365 nm UV light. This characteristic provides an exceptionally convenient method for fluorescence detection: direct visual observation using a portable 365 nm UV lamp.

3.3. Preparation of shape-changing composite fibers

The surface of the layer composed of random PLA/TBC fibrous membranes was further deposited with PU particles by an electrospraying method (Fig. 5a). The deposition density was controlled to be consistent with that of PUP0, PUP1, or PUP2 particles on the PLA/TBC fibrous membranes, which were labeled as shape memory PTP0, PTP1, or PTP2 fibrous membranes, respectively. Random fibers loaded with pristine PUP0 or with PUP2 at a uniform density were also fabricated as controls samples, and the PUP1 deposition density was kept the same as that used for PTP1. PLA/TBC, PTP0, PTP1, and PTP2 fibrous membranes all exhibited a random fibrous morphology in their original shapes (Fig. S3). Specifically, PLA molecular chain entanglements and crystalline domains serve as the permanent phase responsible for storing the original shape, while the TBC-plasticized amorphous PLA segments act as the switching phase. When heated above the glass transition temperature (T_g), the mobility of the PLA chain segments increases, allowing the material to be deformed into a temporary shape. Subsequent cooling below T_g immobilizes the chain segments and fixes the temporary shape. Upon reheating above T_g, the stored elastic strain energy is released, enabling recovery to the original shape. All the different fibrous membranes transformed into an aligned structure in response to specific external stimuli. For the different fibrous membranes loaded with fluorescent PU particles, the particle distribution on the fibrous membranes exhibited greater uniformity after the shape memory recovery process compared to the initial state. The different fibrous membranes were all deformed into a temporarily "U" shape. Subsequently, when placed in warm water at 55 °C, all fibrous membranes recovered to their initial rod-like shape through their thermal-responsive properties (Fig. S4). Meanwhile, the shape memory PTP fibrous membrane exhibits shape fixation and shape recovery ratios of over 95 % (Table S2). Among them, the PTP1 fibrous membrane exhibited the fastest shape recovery rate, with a recovery time of only 10 s (Video 1). By integrating the fibers with PU particles, shape memory fluorescent fibrous membranes exhibit both fluorescence and thermal-

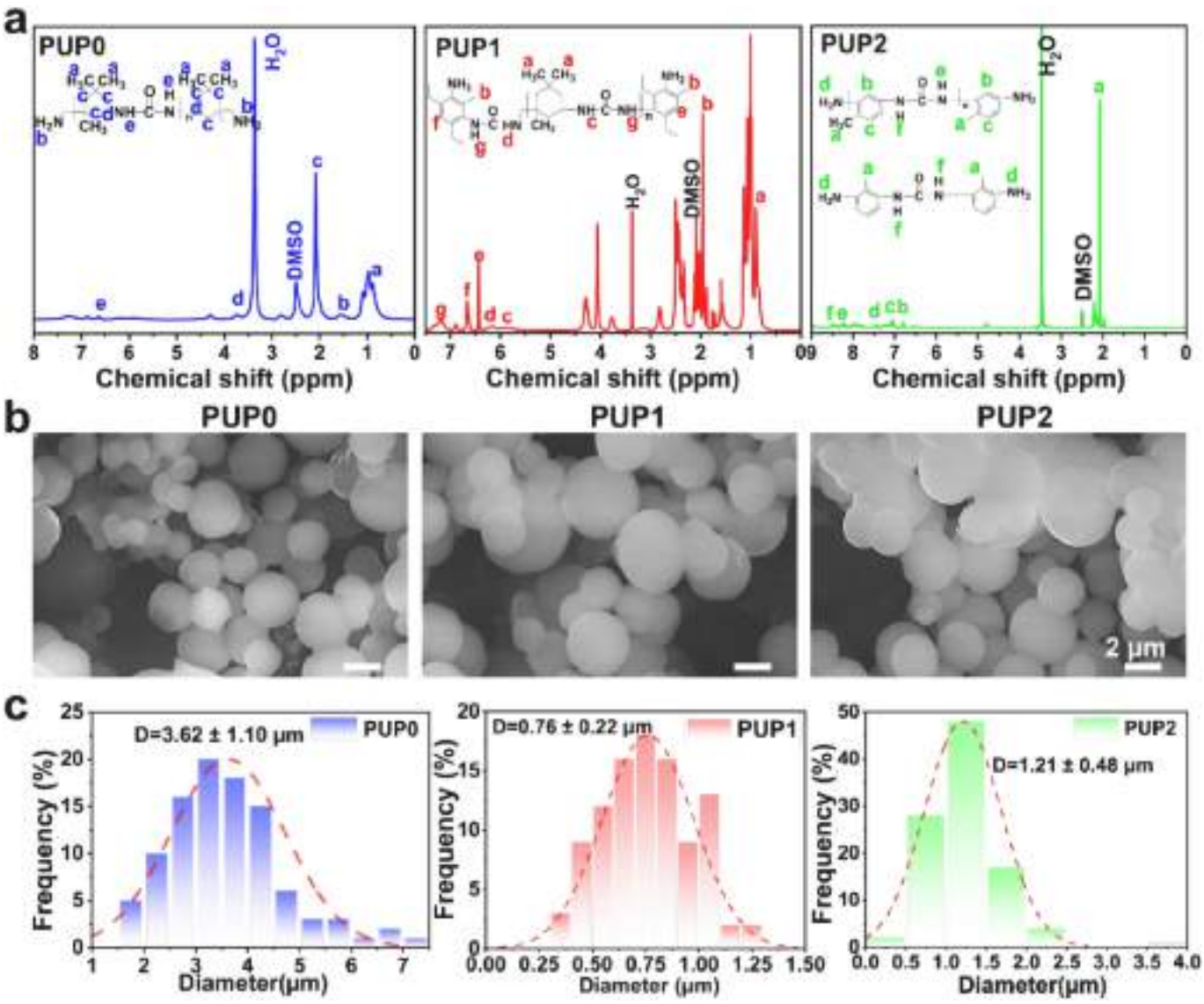

Fig. 3. (a) ^{1}H NMR spectra of PUP0, PUP1, and PUP2. (b) SEM images of PUP0, PUP1, and PUP2. (c) Particle size distribution from SEM statistical analysis.

responsive properties. Fig. 5b displayed SEM images of PLA/TBC, PTP0, PTP1, and PTP2 fibrous membranes, illustrating their structural progression from the initial state during shape memory recovery process. Before deformation, all fibrous membranes exhibited a random microstructure. After deformation, PLA/TBC, PTP0, PTP1, and PTP2 fibrous membranes recovered upon heating from the temporary aligned architecture. During the transition between the temporary and permanent shapes, PLA entered a metastable state in which polymer chains gained mobility, thereby enabling chain rearrangement [45].

Electrospun fibrous membranes with thermal-responsive properties can respond to temperature changes to achieve microscale reversible pore size variations [46]. Electrostatically sprayed particles are deposited onto the fiber membrane, with the distance between particles increasing as particle size increases [47]. Before deformation, the average pore sizes of PLA/TBC, PTP0, PTP1, and PTP2 fibrous membranes were 8, 6, 6, and 7 nm, respectively (Table S3). After deformation, the average pore sizes of PLA/TBC, PTP0, PTP1, and PTP2 fibrous membranes were 13, 11, 8, and 11 nm, respectively (Table S3). Compared to PUP0 and PUP2, particles prepared from PUP1 exhibit the smallest diameter. Consequently, under electrostatic forces, fluorescent PU particles bind more uniformly to the fiber membrane during the construction of PTP fibrous membranes, resulting in smaller pore sizes. In contrast to the random PTP fibrous membrane, the aligned structure exhibits micro-scale reversible pore size changes due to its thermal-responsive properties. Thus, the aligned structure exhibits increased pore size after deformation.

Reducing the fiber diameter in electrospun fiber membranes increases the surface area [48]. Through shaping, the microstructure of PTP fibrous membranes undergoes transformation while simultaneously increasing the specific surface area when subjected to external forces. After shaping to achieve an aligned morphology, PTP fibrous membranes exhibited a 2- to 4-fold increase in specific surface area and pore volume compared to the random morphology (Fig. 5c, Fig. S5, Table S3 and Table S4). Compared with the random fibers, the specific surface area of the shape memory fluorescent PTP fibrous membranes increased, and the pore size distribution changed, thereby promoting the uniform dispersion of particles and enhancing the filtration of Fe^{3+}.

3.4. Properties of the programmable, fluorescent, and shape-changing composite fibers

Owing to strong hydrogen bonding, PU particles do not exhibit a distinct glass transition [49]. In polymer-particle composite systems, the incorporation of particles generally leads to an increase in the T_g relative

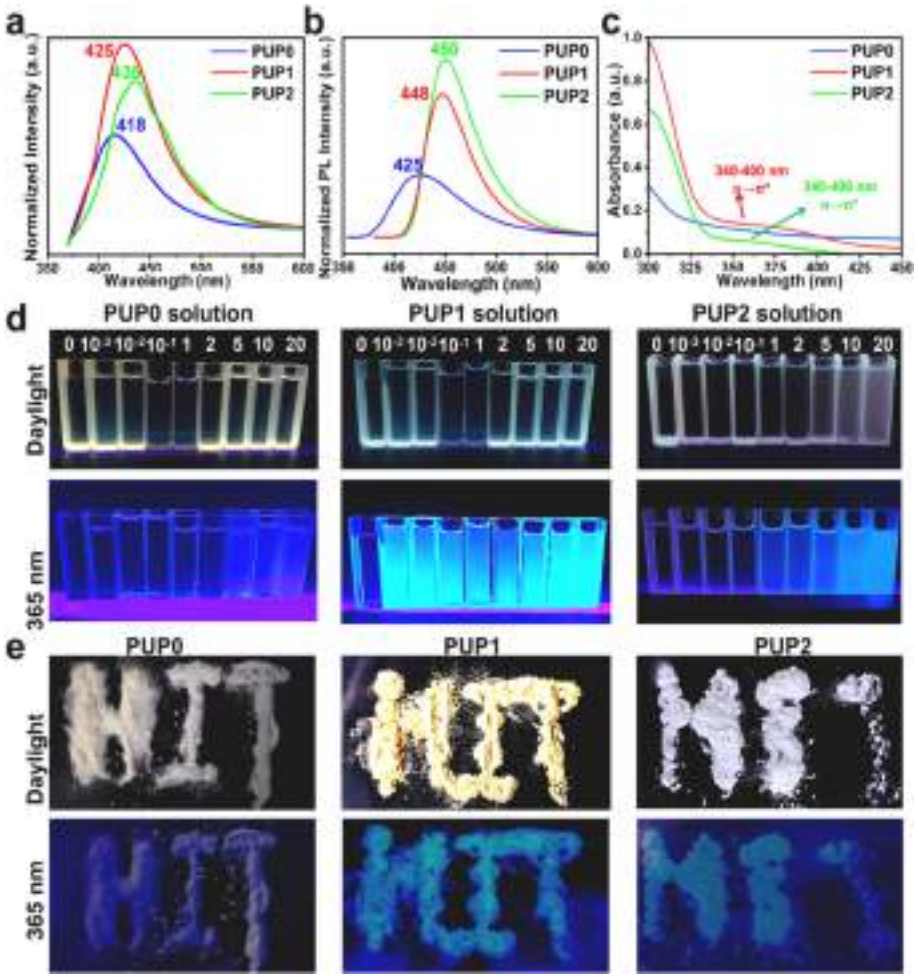

Fig. 4. The fluorescence properties of PUP0, PUP1, and PUP2 are presented as follows: (a) Fluorescence emission spectra of PUP0, PUP1, and PUP2 at an excitation wavelength of 365 nm. (b) Fluorescence emission spectra of PUP0, PUP1, and PUP2 at an excitation wavelength of 430 nm. (c) UV–Vis absorption spectra. (d) Photographs of PUP0, PUP1, and PUP2 at different concentrations dissolved in DMSO/H_2O mixtures, taken under daylight and 365 nm UV light, demonstrating their luminescence in the solution. (e) Photographs of PUP0, PUP1, and PUP2 powder under daylight and 365 nm UV light illumination.

to that of the neat polymer matrix [50]. For particles, T_g may decrease with decreasing particle size due to enhanced interfacial effects and altered chain packing at the polymer-particle interface [34]. The effect of incorporating PU particles into PLA/TBC fibrous membranes on T_g was investigated. Fig. 6a shows the DSC curves of PLA/TBC, PTP0, PTP1, and PTP2 fibrous membranes during the second heating scan. Compared to PLA/TBC, all PU-containing samples exhibited an increase in T_g of more than 5 °C, indicating that PU particles restrict the segmental mobility of polymer chains. Among the composite fibers, PTP1 exhibited a lower T_g than PTP0 and PTP2. This difference may be attributed to particle-size-dependent effects, where smaller particles reduce T_g by modifying interfacial constraints and disrupting local chain packing. PU particles have been reported to exhibit high thermal stability in previous studies [51]. The initial thermal degradation temperature of the fibrous membranes was 300 °C, which is significantly higher than the standard condition of high-pressure sterilization (Fig. 6b). This indicates that the fibrous membranes possess excellent thermal stability and potential adaptability to sterilization processes. PLA/TBC fibrous membranes exhibited stable shape memory performance over five consecutive thermomechanical cycles (Fig. 6c). During cyclic heating and cooling, the strain response consistently tracked the temperature variation, indicating a reliable and reversible recovery process. The results further suggest that temperature-induced molecular chain mobility within the PLA/TBC matrix enables repeated transitions between random and aligned structures, thereby facilitating programmable fibers.

Fibers have attracted significant attention in polluted water treatment due to their high porosity, hydrophilic and small pore size [52]. However, their hydrophobic properties limit their application under the pressures required for polluted water treatment. Surface modification using low-vacuum plasma treatment has been employed to impart hydrophilic properties to shape memory fluorescent PTP fibrous membranes, thereby improving their interfacial wettability. All samples exhibited excellent flexibility and deformability at room temperature (Fig. 6d). At 80 °C, the neat PLA/TBC matrix showed the lowest tensile strength and elongation at break. PTP0 marginally increased strength but reduced elongation, suggesting embrittlement. PTP1 delivered the highest strength improvement while also increasing elongation relative to the neat blend, demonstrating concurrent strengthening and toughening. PTP2 offered a moderate strength increase but a dramatic rise in elongation at break, exhibiting the most significant toughening effect, ideal for high-ductility requirements (Fig. S6).

Notably, the electrospraying of PU particles onto PTP fibrous membranes did not lead to any significant alteration in the mechanical properties of the PLA/TBC matrix. After plasma treatment, the hydrophilicity of the different fibrous membranes was significantly improved. Among them, the water contact angle of PTP1 fibrous membranes was reduced to 26 ± 5°, indicating that plasma treatment can effectively introduce hydrophilic groups or improve surface energy on the fibrous membranes, thereby significantly enhancing the surface hydrophilicity of the materials (Fig. 6e-f). Plasma treatment resulted in improved

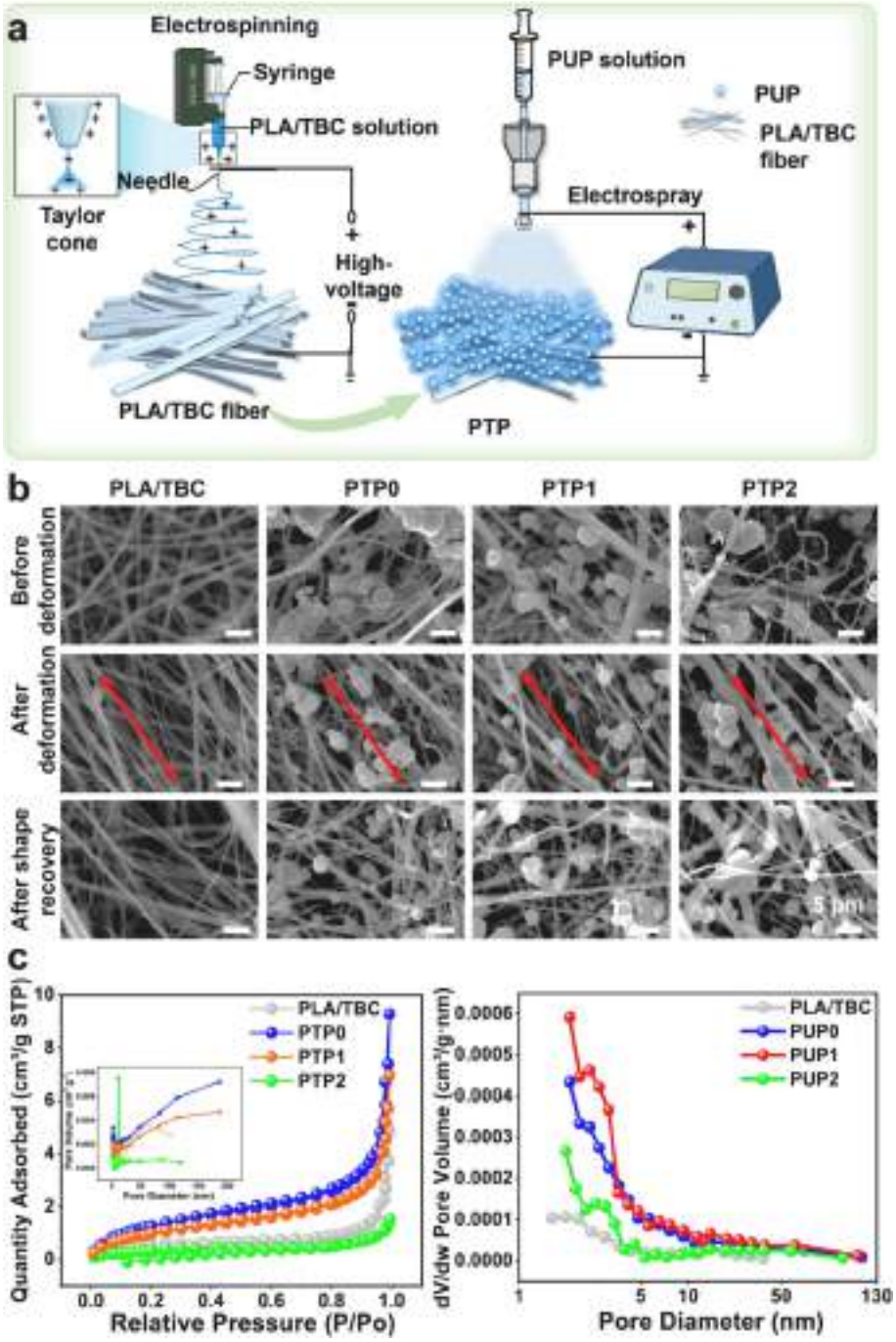

Fig. 5. (a) Fabrication schematic of shape-memory fluorescent composite fibers. (b) SEM images of the different fibrous membranes. The red arrows show the direction of aligned PLA/TBC fibrous membranes. Scale bar = 5 μm. (c) BET analysis after deformation.

surface wettability of the shape memory PTP fibrous membranes, leading to water contact angles decreasing to similar values.

3.5. *Programmable, fluorescent and shape-changing composite fibers for Fe^{3+} detection and filtration*

The stability of metal complexes usually increases with the charge-to-radius ratio of the metal ion. Consequently, Fe^{3+}, with its relatively high charge-to-radius ratio, exhibits strong coordination interactions with PU particles, effectively quenching their molecular fluorescence. Fe^{3+} undergoes a complexation reaction with PU particles, which induces pronounced fluorescence quenching and a significant decrease in fluorescence intensity (Fig. 7a). The high filtration capacity of the PTP composite fibers toward Fe^{3+} is mainly attributed to the stronger coordination interaction and/or electrostatic attraction between Fe^{3+} and the surface functional groups of the fibrous membranes. SEM coupled with energy-dispersive X-ray spectroscopy (EDS) revealed that the different composite fibers were loaded with a significant amount of iron, while no calcium was detected (Fig. 7b). After stretching, the filtration performance of the PTP1 fiber membrane reached 98 %, representing a 32 % increase over the unstretched random fiber membrane. This improvement is attributed to the gradual orientation of the fibers along a specific direction and the optimization of the membrane's internal pore structure, thereby enabling more efficient Fe^{3+} retention (Fig. 7c).

Ca^{2+} was selected as the reference ion to evaluate the selective filtration performance of PTP1 fibrous membranes in complex ionic

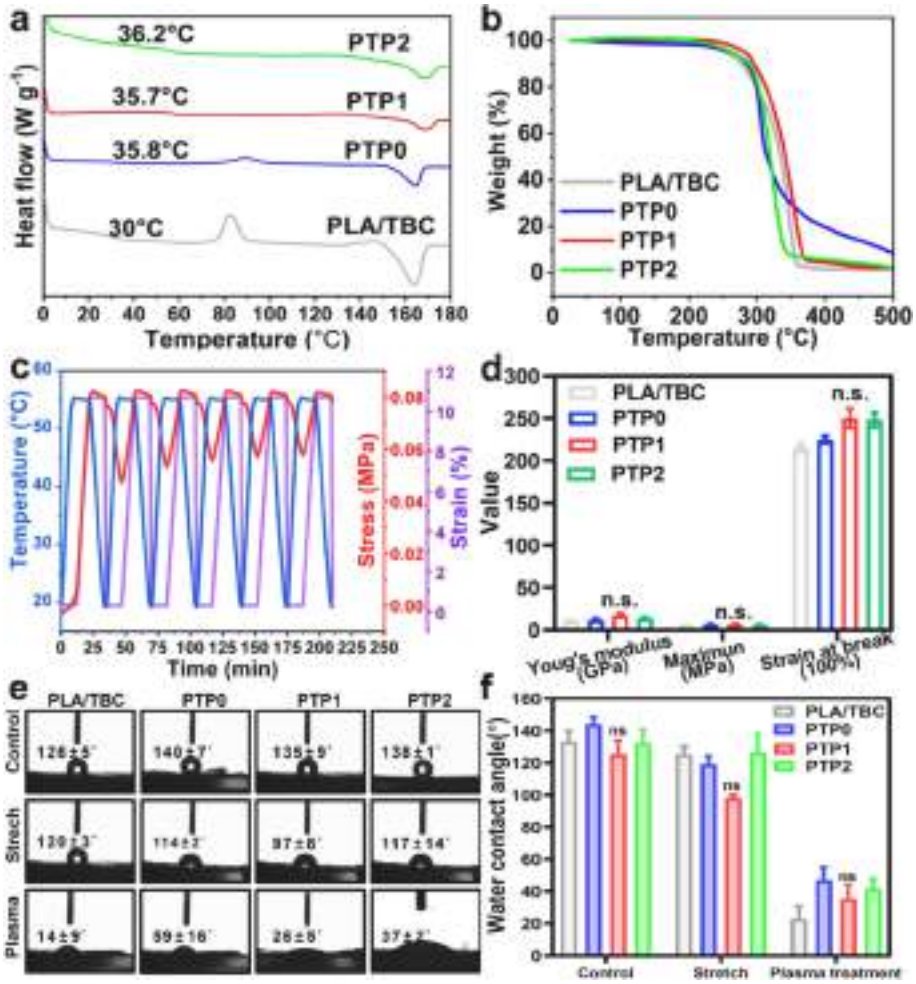

Fig. 6. (a) DSC curves of PLA/TBC, PTP0, PTP1, and PTP2 during the second heating process. (b) TGA curves. (c) The curves of dynamic mechanical analysis. (d) Mechanical properties of the different fibrous membranes at room temperature. (e) Water contact angle before/after deformation and after plasma treatment. (f) The statistical graph of water contact angles (n = 3).

environments. The results indicate that the PTP1 fibrous membranes effectively suppress Ca^{2+} interference while exhibiting a pronounced affinity toward Fe^{3+}. Compared with the PLA/TBC group, the Fe^{3+} removal efficiency of PTP1 increased significantly, whereas the transmembrane flux remained within an acceptable range, suggesting that enhanced selectivity is achieved without a substantial compromise in permeation performance. This behavior can be attributed to the strong and specific complexation ability between Fe^{3+} and PUP1 embedded in the fibrous membrane. In contrast, negligible coordination or specific interaction occurs between Ca^{2+} and the shape memory fluorescent PTP fibrous membranes, resulting in an almost unchanged fluorescence response during filtration (Fig. 7d). Fig. S7 and Fig. S8 demonstrated that $FeCl_3$ induces a significantly specific fluorescence quenching compared with all other tested ions, confirming the excellent selectivity of the composite fiber membrane toward Fe^{3+}. As shown in Fig. 7e, new characteristic signal appeared in the XPS spectra of the shape memory fluorescent PTP0, PTP1, and PTP2 fibrous membranes after Fe^{3+} filtration, confirming the formation of C=O-Fe coordination complexes within the PU particles.

A detailed comparison of the C 1 s spectra before and after filtration reveals a decrease in the electron density associated with the carbonyl oxygen, consistent with electron donation from C=O groups to Fe^{3+}. This change verifies the formation of C=O-Fe coordination bonds (Fig. S9) and further supports the selective complexation mechanism between the fluorescent PU particles and Fe^{3+}.

4. Conclusions

In summary, programmable, fluorescent, and shape-changing composite fibers for Fe^{3+} detection and filtration were successfully fabricated via electrospinning combined with the incorporation of functional fluorescent particles. The resulting composite fibers exhibited a selective fluorescence response toward Fe^{3+}, enabling visual monitoring of Fe^{3+} contamination. Strong inter-fiber electrostatic interactions ensured structural integrity and contributed to the multifunctional performance of the composite system. The incorporation of shape memory effect endowed the fibers with programmable structural transformation capability, allowing adaptive regulation of filtration configurations. In addition, the porous fibrous architecture provided efficient Fe^{3+} capture and filtration performance, demonstrating the feasibility of integrating detection and removal functions within a single material platform. Overall, this multifunctional strategy offers a promising approach for the development of smart water-treatment materials with potential applications in environmental monitoring and precision wastewater remediation.

CRediT authorship contribution statement

Yiling Yu: Writing – original draft. **Tao Guo:** Data curation. **Lan Luo:** Data curation. **Linlin Wang:** Writing – review & editing. **Fenghua Zhang:** Writing – review & editing. **Yanju Liu:** Funding acquisition. **Jinsong Leng:** Funding acquisition.

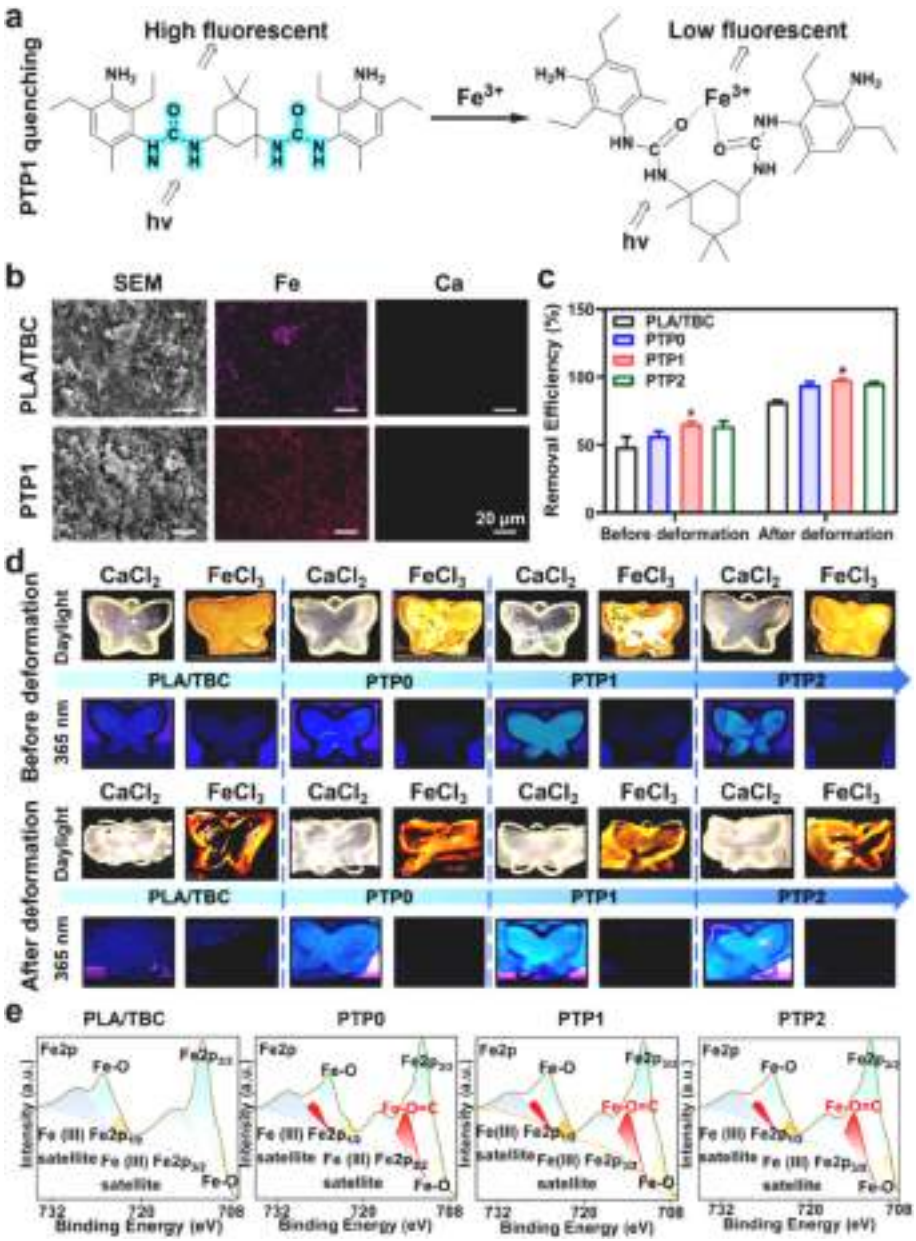

Fig. 7. (a) Schematic illustration of the fluorescence quenching of PUP1. (b) SEM/EDS characterization of surface morphology and element distribution of the different fibrous membranes after filtering different ionic solutions. Scale bar = 20 μm. (c) Statistical graph of Fe^{3+} removal efficiency (n = 3). (d) Images of the 5 s filtration process of $FeCl_3$ and $CaCl_2$ solutions using the different fibrous membranes. (e) XPS spectra after filtration.

Declaration of competing interest

The authors declare that they have no known competing financial interests or personal relationships that could have appeared to influence the work reported in this paper.

Acknowledgments

This research was supported by the Heilongjiang Provincial Natural Science Foundation of China (Grant 2022ZX02C25).

Appendix A. Supplementary data

Supplementary data to this article can be found online at https://doi.org/10.1016/j.compositesa.2026.110083.

Data availability

Data will be made available on request.

References

[1] Alorabi AQ. Recent developments in colorimetric and fluorimetric sensing of Fe^{2+} and Fe^{3+} ions: a review (2021 to 2025). Crit Rev Anal Chem 2025:1–18. https://doi.org/10.1080/10408347.2025.2531970.
[2] Liu B, He W, Lu H, et al. A facile design for multifunctional AIEgen based on tetraaniline derivatives. Sci China Chem 2019;62:732–8. https://doi.org/10.1007/s11426-018-9440-0.
[3] Liu S, Yin J, Wan D, Yin Y. The role of iron in intestinal mucus: perspectives from both the host and gut microbiota. Adv Nutr 2024;15:100307. https://doi.org/10.1016/j.advnut.2024.100307.
[4] Yang XL, Wang PY, Yang H, et al. A portable and selective fluorescent probe based on sodium alginate for simultaneous detection and adsorption of Fe^{3+}. Int J Biol Macromol 2026;339:150036. https://doi.org/10.1016/j.ijbiomac.2025.150036.

[5] Shumoy H, Raes K. Dissecting the facts about the impact of contaminant iron in human nutrition: a review. Trends Food Sci Technol 2021;116:918–27. https://doi.org/10.1016/j.tifs.2021.08.038.

[6] Wang YQ, Hou YQ, Huo FW, et al. Fe^{3+} ion quantification with reusable bioinspired nanopores. Chin Chem Lett 2025;36:110428. https://doi.org/10.1016/j.cclet.2024.110428.

[7] Issa MA, Abidin ZZ, Sobri S, et al. Fluorescent recognition of Fe^{3+} in acidic environment by enhanced-quantum yield N-doped carbon dots: optimization of variables using central composite design. Sci Rep 2020;10:11710. https://doi.org/10.1038/s41598-020-68390-8.

[8] Chaturvedi S, Dave PN. Removal of iron for safe drinking water. Desalination 2010;303:1–11. https://doi.org/10.1016/j.desal.2012.07.003.

[9] Catapano A, Cimmino F, Petrella L, et al. Iron metabolism and ferroptosis in health and diseases: the crucial role of mitochondria in metabolically active tissues. J Nutr Biochem 2025;140:109888. https://doi.org/10.1016/j.jnutbio.2025.109888.

[10] Allison SC, Patricio HR, William AS, et al. Chronic toxicity of iron to aquatic organisms under variable pH, hardness, and dissolved organic carbon conditions. Environ Toxicol Chem 2023;42:1371–85. https://doi.org/10.1002/etc.5627.

[11] Zhang Z, An CC, Feng LY, et al. Highly sensitive, selective and reversible detection of Fe^{3+} ions based on elastic cellulose nanofibrils/chitosan composite modified with colorimetric and fluorescent probe. Carbohydr Polym 2026;375:124761. https://doi.org/10.1016/j.carbpol.2025.124761.

[12] Masud MAA, Samaraweera H, Mondol MMH, et al. Iron biochar synergy in aquatic systems through surface functionalities electron transfer and reactive species dynamics. npj Clean Water 2025;8:46. https://doi.org/10.1016/j.jnutbio.2025.109888.

[13] Van Acker T, Theiner S, Bolea-Fernandez E, et al. Inductively coupled plasma mass spectrometry. Nat Rev Methods Primers 2023;3:52. https://doi.org/10.1038/s43586-023-00235-w.

[14] Chen B, Yu P, Chan WN, et al. Cellular zinc metabolism and zinc signaling: from biological functions to diseases and therapeutic targets. Sig Transduct Target Ther 2024;9:6. https://doi.org/10.1038/s41392-023-01679-y.

[15] Kanu AB. Recent developments in sample preparation techniques combined with high-performance liquid chromatography: a critical review. J Chromatogr A 2021;1654:462444. https://doi.org/10.1016/j.chroma.2021.462444.

[16] Wang BY, Guo LJ, Yan XT, et al. Dual-mode detection sensor based on nitrogen-doped carbon dots from pine needles for the determination of Fe^{3+} and folic acid. Spectrochim Acta A 2023;285:121891. https://doi.org/10.1016/j.saa.2022.121891.

[17] Zhang Y, Zhu Y, Zeng ZT, et al. Sensors for the environmental pollutant detection: are we already there? Coord Chem Rev 2021;431:213681. https://doi.org/10.1016/j.ccr.2020.213681.

[18] Qiu C, Liu H, Wang X, et al. Cellulose-based fluorescent chemosensor with controllable sensitivity for Fe^{3+} detection. Carbohydr Polym 2024;346:122620. https://doi.org/10.1016/j.carbpol.2024.122620.

[19] Huang JL, Zhou SH, Zhang SY, et al. Two-dimensional layered MOF nanosheets with multiple binding sites for selective detection and removal of Fe (III) ions. Sep Purif Technol 2024;336:126294. https://doi.org/10.1016/j.seppur.2024.126294.

[20] Wang D, Zhang WQ, Zhou S, et al. A novel dual-functional coordination polymer for detection and ultra-effectively removal of Fe (III) in water. J Mol Liq 2022;355:118942. https://doi.org/10.1016/j.molliq.2022.118942.

[21] Li LF, Cui X, Luo RZ, et al. Piezoelectric electrospun fibers for tissue regeneration: synergizing microarchitecture and enhancement strategies. Sci Bull 2026;71:857. https://doi.org/10.1016/j.scib.2025.12.031.

[22] Jin BH, Yu YL, Lou CH, et al. Combining a density gradient of biomacromolecular nanoparticles with biological effectors in an electrospun fiber-based nerve guidance conduit to promote peripheral nerve repair. Adv Sci 2022;10:2203296. https://doi.org/10.1002/advs.202203296.

[23] Wang L, Ma JY, Guo T, et al. Control of surface wrinkles on shape memory PLA/PPDO micro-nanofibers and their applications in drug release and anti-scarring. Adv Fiber Mater 2023;5:632–49. https://doi.org/10.1007/s42765-022-00249-1.

[24] Wang L, Zhang FH, Liu YJ, et al. Shape memory polymer fibers: materials, structures, and applications. Adv Fiber Mater 2022;4:5–23. https://doi.org/10.1007/s42765-021-00073-z.

[25] Bai YF, Zhu SY, Liang J, et al. 4D Printing of magnetically responsive materials and their applications. Research 2025;8(0847). https://doi.org/10.34133/research.0847.

[26] Yu YL, Zhang FH, Liu YJ, et al. Smart polymer fibers: promising advances in microstructures, stimuli-responsive properties and applications. Adv Fiber Mater 2025;7:1010–41. https://doi.org/10.1007/s42765-025-00539-4.

[27] Liu W, Zhao W, Xie K, et al. Toughening and responsive contractile shape memory fibrous membrane via water for mechanically active wound dressing. Adv Fiber Mater 2024;6:1942–54. https://doi.org/10.1007/s42765-024-00463-z.

[28] Han YL, Geng QW, Dong A, et al. Anti-scar effects of micropatterned hydrogel after glaucoma drainage device implantation. Research 2025;8(0561). https://doi.org/10.34133/research.0561.

[29] Li QY, Chen L, Yu J, et al. Inhibiting cell inspection points intervention via injectable short fibers for reversing neural cell senescence. Adv Fiber Mater 2025;7:1766–87. https://doi.org/10.1007/s42765-025-00513-0.

[30] Jiang SJ, Zhou JL, Zhao CC, et al. Aligned electrospun fibers inducing cell and nuclear morphology remodeling via ras-associated protein 1/yes-associated protein signaling enhances bone regeneration. Adv Fiber Mater 2025;7:1980–97. https://doi.org/10.1007/s42765-025-00596-9.

[31] Kavarthapu VS, Manchi P, Kurakula A, et al. Flexible electrospun PDMS/PVDF-HFP composite nanofibers-based hybrid nanogenerators for efficient mechanical energy harvesting and multi-sensing applications. Adv Fiber Mater 2025;8:655–70. https://doi.org/10.1007/s42765-025-00638-2.

[32] Gong RX, Dong YJ, Ge D, et al. Wet spinning fabrication of robust and uniform intrinsically conductive cellulose nanofibril/Silk conductive fibers as bifunctional strain/humidity sensor in potential smart dressing. Adv Fiber Mater 2024;6:993–1007. https://doi.org/10.1007/s42765-024-00404-w.

[33] Xu X, Lv H, Zhang M, et al. Recent progress in electrospun nanofibers and their applications in heavy metal wastewater treatment. Front Chem Sci Eng 2023;17:249–75. https://doi.org/10.1007/s11705-022-2245-0.

[34] Wang HM, Zhan BB, Zhang YR, et al. Multi-scale synergistic regulation strategy to develop mesoporous carbon hollow nanospheres/bean-shaped nanofibers for corrosion-resistant, flexible, and lightweight microwave absorbers. Research 2025;9(2639–5274). https://doi.org/10.34133/research.1051.

[35] Cui JX, Li FH, Wang YL, et al. Electrospun nanofiber membranes for wastewater treatment applications. Sep Purif Technol 2020;250:117116. https://doi.org/10.1016/j.seppur.2020.117116.

[36] Kachal V, Tan JC. Stimuli-responsive electrospun fluorescent fibers augmented with aggregation-induced emission (AIE) for smart applications. Adv Sci 2022;10:2204848. https://doi.org/10.1002/advs.202204848.

[37] Hu LK, Zhang FH, Luo L, et al. Advances in shape memory polymer porous materials: Fabrications, microstructures, and applications. Research 2025;8(0989). https://doi.org/10.34133/research.0989.

[38] Somarathna Y, Herath M, Islam MM, et al. Chemo-rheological optimization of hot-melt epoxy resin systems for shape memory polymer smart prepregs. Compos A Appl Sci Manuf 2026;207:109812. https://doi.org/10.1016/j.compositesa.2026.109812.

[39] Li L, Wang X, Huang C, et al. 3D printed shape memory polyimide composite aerogels with CNT-directed thermal networks for rapid shape recovery. Compos A Appl Sci Manuf 2026;203:109586. https://doi.org/10.1016/j.compositesa.2026.109586.

[40] Tang Z, Zhang X, Su L, et al. Ablation-resistant shape memory polyimide composite aerogels with exceptional high temperature response for smart thermal protection. Compos A Appl Sci Manuf 2026;203:109570. https://doi.org/10.1016/j.compositesa.2026.109570.

[41] Chen YJ, Liu JH, Li XH, et al. Mesoporous silica-loaded phosphorus-modified hexadecanol nanocomposites for flame-retardant and shape-stabilized phase change materials. Compos A Appl Sci Manuf 2025;199:109227. https://doi.org/10.1016/j.compositesa.2025.109227.

[42] Cao HY, Li B, Jiang XH, et al. Fluorescent linear polyurea based on toluene diisocyanate: easy preparation, broad emission and potential applications. Chem Eng J 2020;399:125867. https://doi.org/10.1016/j.cej.2020.125867.

[43] Yuan Z, Yan J, Gao F, et al. High-performance, fluorescent, UV-shielding, triboelectric, super-flexible polyurea elastomers via strong π-π stacking of pyrene and hydrogen bonding strategies. J Mater Chem C 2023;11:8971–81. https://doi.org/10.1039/D3TC00963G.

[44] Li PC, Zhao HZ, Liu ZL, et al. A high-toughness NDI-based fluorescent polyurea based on gradient energy dissipation. Macromolecules 2025;58:3774–86. https://doi.org/10.1021/acs.macromol.4c02637.

[45] Delaey J, Dubruel P, Vlierberghe SV. Shape-memory polymers for biomedical applications. Adv Funct Mater 2020;30:1909047. https://doi.org/10.1002/adfm.201909047.

[46] Zhang QC, Rudolph T, Benitez AJ, et al. Temperature-controlled reversible pore size change of electrospun fibrous shape-memory polymer actuator based meshes. Smart Mater Struct 2019;28:055037. https://doi.org/10.1088/1361-665X/ab10a1.

[47] Raghuwanshi VS, Garusinghe UM, Ilavsky J, et al. Effect of nanoparticles size and polyelectrolyte on nanoparticles aggregation in a cellulose fibrous matrix. J Colloid Interface Sci 2018;510:190–8. https://doi.org/10.1016/j.jcis.2017.09.064.

[48] Eichhorn SJ, Sampson WW. Relationships between specific surface area and pore size in electrospun polymer fibre networks. J R Soc Interface 2010;7:641–9. https://doi.org/10.1098/rsif.2009.0374.

[49] Han H, Li SS, Zhu XL, et al. One step preparation of porous polyurea by reaction of toluene diisocyanate with water and its characterization. RSC Adv 2014;4:33520–9. https://doi.org/10.1039/C4RA06383J.

[50] Bamford JT, Smith RA, Leng CZ, et al. Measuring the glass transition temperature of vapor-phase-infiltrated AlOx-PS-r-PHEMA organic-inorganic hybrid thin-film materials. Macromolecules 2021;54:6790–8. https://doi.org/10.1021/acs.macromol.1c00691.

[51] Zhang Z, Shi HX, Jiang Q. Glass transition of organic nanoparticles. Mater Lett 2000;44:261–4. https://doi.org/10.1016/S0167-577X(00)00040-9.

[52] Yalcinkaya F, Yalcinkaya B, Pazourek A, et al. Surface modification of electrospun PVDF/PAN nanofibrous layers by low vacuum plasma treatment. Int J Polym Sci 2016;9:4671658. https://doi.org/10.1155/2016/4671658.